



# Greatly Improved Conductivity of Double-Chain Polymer Network Binder for High Sulfur Loading Lithium–Sulfur Batteries with a Low Electrolyte/Sulfur Ratio

Xuejun Liu, Tao Qian,\* Jie Liu, Jinghua Tian, Li Zhang, and Chenglin Yan\*

Binders have been considered to play a key role in realizing high-energy-density lithium–sulfur batteries. However, the accompanying problems of limited conductivity and inferior affinity of soluble polysulfide intermediates bring down their comprehensive performance for practical applications. Herein, the synthesis of a novel double-chain polymer network (DCP) binder by polymerizing 4,4'-biphenyldisulfonic acid connected pyrrole monomer onto viscous sodium carboxymethyl cellulose matrix, yielding a primary crystal structure is reported. Consequently, the resulted binder enables superior rate performance from 0.2 C (1326.9 mAh g<sup>-1</sup>) to 4 C (701.4 mAh g<sup>-1</sup>). Moreover, a high sulfur loading of 9.8 mg cm<sup>-2</sup> and a low electrolyte/sulfur ratio (5:1, μL mg<sup>-1</sup>) are achieved, exhibiting a high area capacity of 9.2 mAh cm<sup>-2</sup>. In situ X-ray diffraction analysis is conducted to monitor the structural modifications of the cathode, confirming the occurrence of sulfur reduction/recrystallization during charge–discharge process. In addition, in situ UV–vis measurements demonstrate that DCP binder impedes the polysulfide migration, thereby giving rise to high capacity retention for 400 cycles.

The rapid development of portable devices and electric vehicles stimulates the search for rechargeable batteries with high energy density. Lithium–sulfur (Li–S) batteries with superior theoretical capacity (1675 mAh g<sup>-1</sup>) are regarded as promising candidates for the next generation rechargeable battery technology.<sup>[1]</sup> However, Li–S batteries still suffer from some formidable problems, mainly originating from low conductivity of sulfur and its discharge product together with lithium polysulfide dissolution and shuttling.<sup>[2]</sup> Although encapsulating sulfur within conductive carbon hosts (S/C) has been developed to solve the above issues, majority of the current works

are targeted at a low sulfur loading of less than 2 mg cm<sup>-2</sup>.<sup>[3]</sup> Increasing sulfur loading results in the crack and delamination of cathode materials from current collector.<sup>[4]</sup> In addition, due to the large void space inside and/or large fraction of non-active carbons, the high sulfur loadings are realized at the cost of high electrolyte/sulfur ratios which are used to fully wet the electrodes.<sup>[5]</sup> So it is still critical to construct feasible Li–S batteries with high sulfur loading and low electrolyte/sulfur ratio.

For the traditional slurry-based process, binders with sufficient adhesivity and elasticity are essential to bond active materials and conductive additives together. As one of the most common binders, polyvinylidene fluoride (PVDF) has been widely used for Li–S batteries. However, the nonfunctionalized linear chain structure cannot afford sufficient adsorption

to the soluble polysulfide intermediates, resulting in the rapid capacity decay.<sup>[6]</sup> Thus alternatives with polar functional groups to restrict polysulfide dissolution are highly desirable.<sup>[7]</sup> In the meantime, an even more challenging issue is how to increase the mass loading and area capacity to maximize its energy density. Various polymers, such as carbonyl-β-cyclodextrin,<sup>[8]</sup> poly(ethylene oxide),<sup>[9]</sup> and gelatin<sup>[10]</sup> have been applied to replace conventional PVDF binder, leading to improved electrochemical performance. Unfortunately, all these materials are poor electronic conductors, resulting in reduced energy density.

Hence, we demonstrate that high-energy-density batteries can be achieved by exploiting a multifunctional double-chain polymer network (DCP) binder, which is composed of sodium carboxyl methyl cellulose (CMC) and 4,4'-biphenyldisulfonic acid connected polypyrrole (Sul-PPy). The benefits of this binder for high energy storage are multifold. The water-soluble, viscous CMC matrix endows the cathode with efficient physical connection between particles and high elasticity to accommodate the large volume expansion. Particularly, the Sul-PPy polymers form an electrically percolating network within the CMC matrix. It should be noted that the addition of a little Sul-PPy (<6.4 wt%) within CMC endows the DCP binder with reduced resistance, and thus contributing greatly to the electrical conductivity of sulfur@double-chain polymer network (S@DCP) cathodes. From four-point probe measurements, it is shown that the

X. Liu, Dr. T. Qian, J. Liu, Prof. J. Tian, Prof. L. Zhang, Prof. C. Yan  
Soochow Institute for Energy and Materials Innovations  
College of Physics  
Optoelectronics and Energy  
Collaborative Innovation Center of Suzhou Nano Science and  
Technology  
Key Laboratory of Advanced Carbon Materials and Wearable Energy  
Technologies of Jiangsu Province  
Soochow University  
Suzhou 215006, China  
E-mail: tqian@suda.edu.cn, c.yan@suda.edu.cn

The ORCID identification number(s) for the author(s) of this article can be found under <https://doi.org/10.1002/smll.201801536>.

DOI: 10.1002/smll.201801536

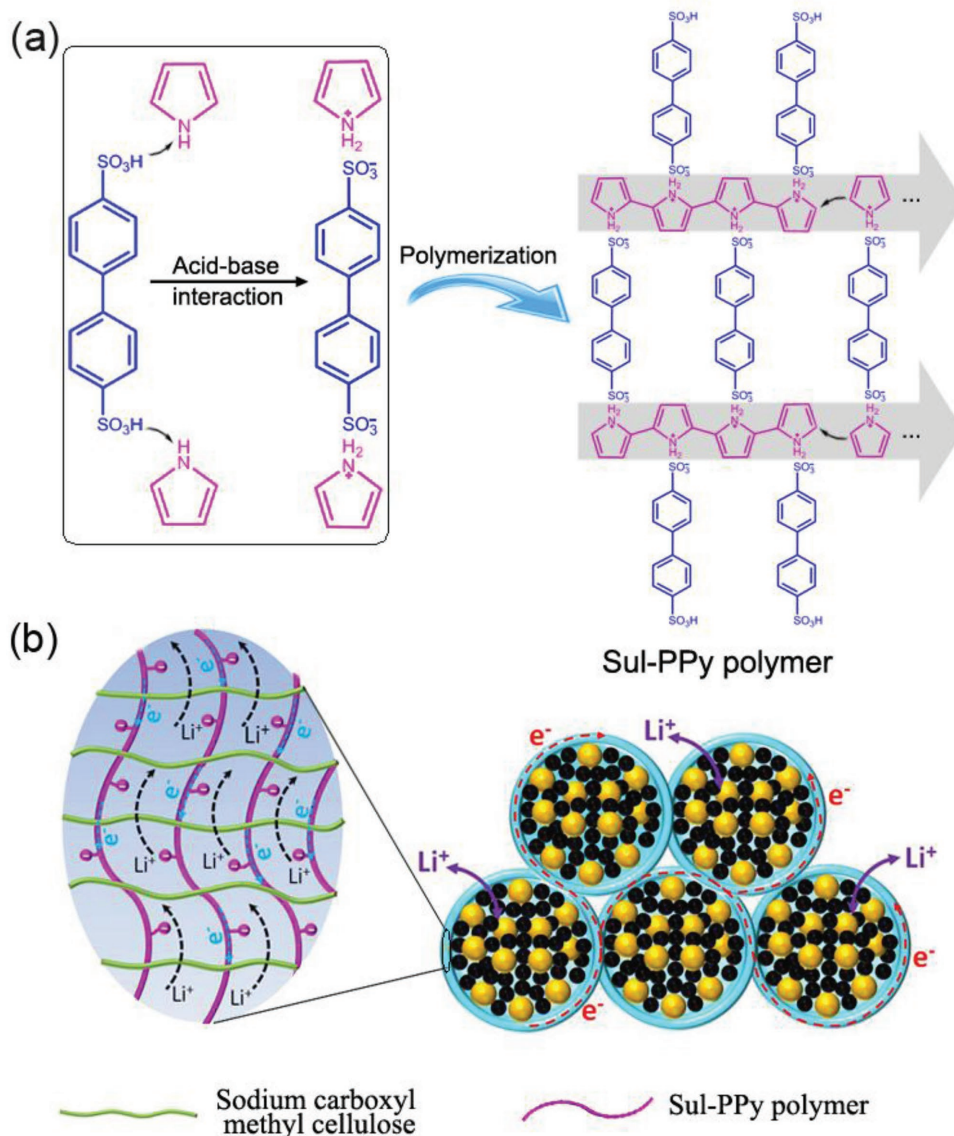


**Figure 1.** a) Chemical oxidative polymerization of 4,4'-biphenyldisulfonic acid connected pyrrole, producing crystal Sul-PPy polymers. b) Schematic diagram of the interactions inside the binders with high ion and electron conductivities.

S@DCP cathode ( $0.010 \Omega \cdot \text{cm}$ ) is twice more conductive than sulfur@sodium carboxyl methyl cellulose (S@CMC) cathode, which is much higher than that for sulfur@polyvinylidene fluoride (S@PVDF). Moreover, plenty of sulfonate groups on Sul-PPy provide a negatively charged environment to facilitate lithium ion transport and restrict the migration of negatively charged polysulfide ions within the cathode, which is clearly illustrated by in situ UV-vis measurements. This binder serves multiple functionalities in the electrode, thus excellent rate capability from 0.2 C ( $1326.9 \text{ mAh g}^{-1}$ ) to 4 C ( $701.4 \text{ mAh g}^{-1}$ ) can be achieved. More importantly, crack-free electrodes with high sulfur loading ( $9.8 \text{ mg cm}^{-2}$ ) are obtained, which allows a high area capacity of  $9.2 \text{ mAh cm}^{-2}$ . Using this approach, a relatively low electrolyte/sulfur ratio ( $5:1 \mu\text{L mg}^{-1}$ ) can be obtained. We demonstrate that this binder provides a new binder-design perspective to access high-energy-density Li-S batteries.

Facilitated transport of ions and electrons is critical to construct high-loading electrodes for Li-S batteries. DCP binder was designed by polymerizing 4,4'-biphenyldisulfonic acid connected pyrrole monomer onto the viscous sodium CMC matrix. As shown in Figure 1, the ionic bonding formed between 4,4'-biphenyldisulfonic acid and pyrrole allows directing the polymerization along a certain direction, thus offering convenient electrical conduction pathways to enhance the charge transfer within the cathode materials. Moreover, the negatively charged sulfonate anion groups bound to the polymer backbone are prone to be coupled with the positively charged lithium ion, facilitating fast  $\text{Li}^+$  transport.<sup>[11]</sup> Fourier transform infrared spectroscopy was conducted to identify the chemical bonding of molecular structures. As shown in Figure 2a, apart from the typical signals of CMC ( $1323$  and  $1068 \text{ cm}^{-1}$ ),<sup>[12]</sup> the characteristic peaks of PPy appear at  $1552$  and  $1398 \text{ cm}^{-1}$ , which

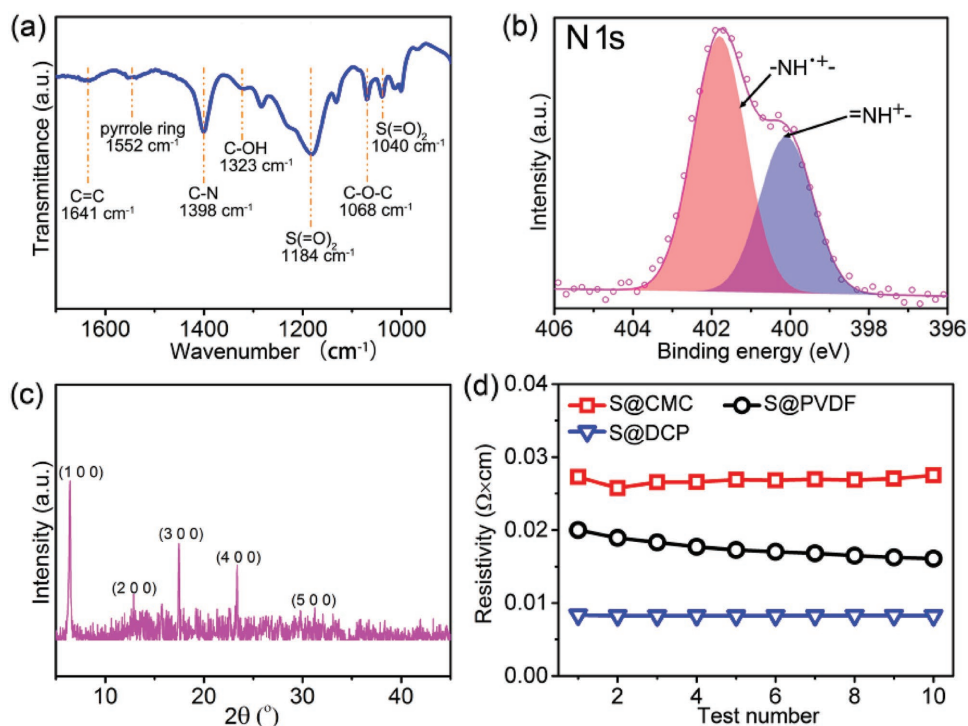


**Figure 2.** a) Fourier transform infrared spectroscopy of the synthesized DCP binder. b) The N 1s signals of DCP binder, indicating the presence of charged Py in the polaron ( $-\text{NH}^{\bullet+}$ , red) and bipolaron ( $=\text{NH}^{\bullet+}$ , blue) states. c) The X-ray diffraction spectrum of DCP binder. d) The results of four-point probe resistivity measurements for S@DCP, S@CMC, and S@PVDF.

are associated with (pyrrole ring [benzenoid ring] stretching) and C–N stretching, respectively.<sup>[13]</sup> The characteristic adsorption peaks for 4,4'-biphenyldisulfonic acid connector are displayed as follows: the peak appearing at  $1641\text{ cm}^{-1}$  corresponds to C=C stretching of the biphenyl ring in the connector.<sup>[14]</sup> The vibration bands at  $1184$  and  $1040\text{ cm}^{-1}$  are believed to be associated with the symmetric/asymmetric  $\text{S}(=\text{O})_2$  stretching.<sup>[13]</sup> X-ray photoelectron spectroscopy was further utilized to illustrate the interaction between PPy and 4,4'-biphenyldisulfonic acid (BSA) connector. As revealed by the N 1s signals of DCP binder (Figure 2b), the presence of charged Py in the polaron ( $-\text{NH}^{\bullet+}$ , red) and bipolaron ( $=\text{NH}^{\bullet+}$ , blue) states clearly shows the direct linkage between pyrrole monomer and the connector via the acid–base interaction.<sup>[14]</sup> When polymerization proceeds with BSA-connected pyrrole (BCP), the reactive sites of the BCP impose restriction on the direction of propagation and thus prevent the randomly oriented chain growth. As shown in Figure 2c, the X-ray diffraction peaks (1 0 0, 2 0 0, 3 0 0, 4 0 0, 5 0 0) agree well with those reported in the literature,<sup>[14]</sup> indicating the crystal structure of Sul-PPy in DCP binder. The crystalline Sul-PPy endows the DCP binder with enhanced electrical conductivity, which is clearly demonstrated in Figure S1 (Supporting Information). The adhesive strength of the DCP binder was characterized and compared with PVDF and CMC. As shown in Figure S2 (Supporting Information), after the peeling test, a large quantity of S@PVDF particles were peeled off the Al foil, while the S@CMC and S@DCP remained the typical black color of S/C composite. This is due to the much higher binding strength for CMC-based electrode compared with PVDF-based electrode.<sup>[15]</sup>

Electrochemical test was conducted to evaluate the application of DCP binder in Li–S batteries. Figure S3 (Supporting Information) demonstrates the cyclic voltammetry curves of S@DCP cathode. Between 1.6 and 2.8 V, the S@DCP cathode exhibits two cathodic peaks and one anodic peak located at  $\approx 2.28$ , 2.01, and 2.42 V, corresponding to the multiple-step reduction of  $\text{S}_8$  and lithium sulfides oxide reaction, respectively. In addition, CV curves of Li–S batteries employing S@PVDF and S@CMC cathodes are also carried out and shown in Figure S4 (Supporting Information). The CV curve of S@DCP cathode displays sharper peaks and lower polarization compared to other electrodes, indicating the enhanced electrochemical kinetics of the S@DCP cathode.<sup>[16]</sup> From the four-point probe measurements (Figure 2d), it can be found that S@DCP ( $0.010\ \Omega\cdot\text{cm}$ ) is more conductive than S@PVDF and S@CMC. Therefore, the S@DCP cathode exhibits superior rate capability from 0.2 to 4 C. As shown in Figure 3a, the highest initial capacity of  $1326.9\text{ mAh g}^{-1}$  (0.2 C) is obtained for the S@DCP cathode. With further cycling at 0.5, 1, 2, and 4 C, the S@DCP cathode shows reversible capacities of 976.0, 885.2, 796.8, and  $701.4\text{ mAh g}^{-1}$ , respectively, which are much higher than that of S@CMC and S@PVDF cathodes. Figure S5 (Supporting Information) shows the galvanostatic charge/discharge profiles of S@DCP, S@PVDF, and S@CMC cathodes. The S@DCP cathode exhibits flat and stable plateaus with lower polarization, demonstrating a kinetically efficient reaction process. In contrast, the overpotential grows larger when the current density is increased and the plateaus shift obviously or even disappear at high current rates for S@PVDF and S@CMC cathodes, indicating slow reaction kinetics and high polarization. In

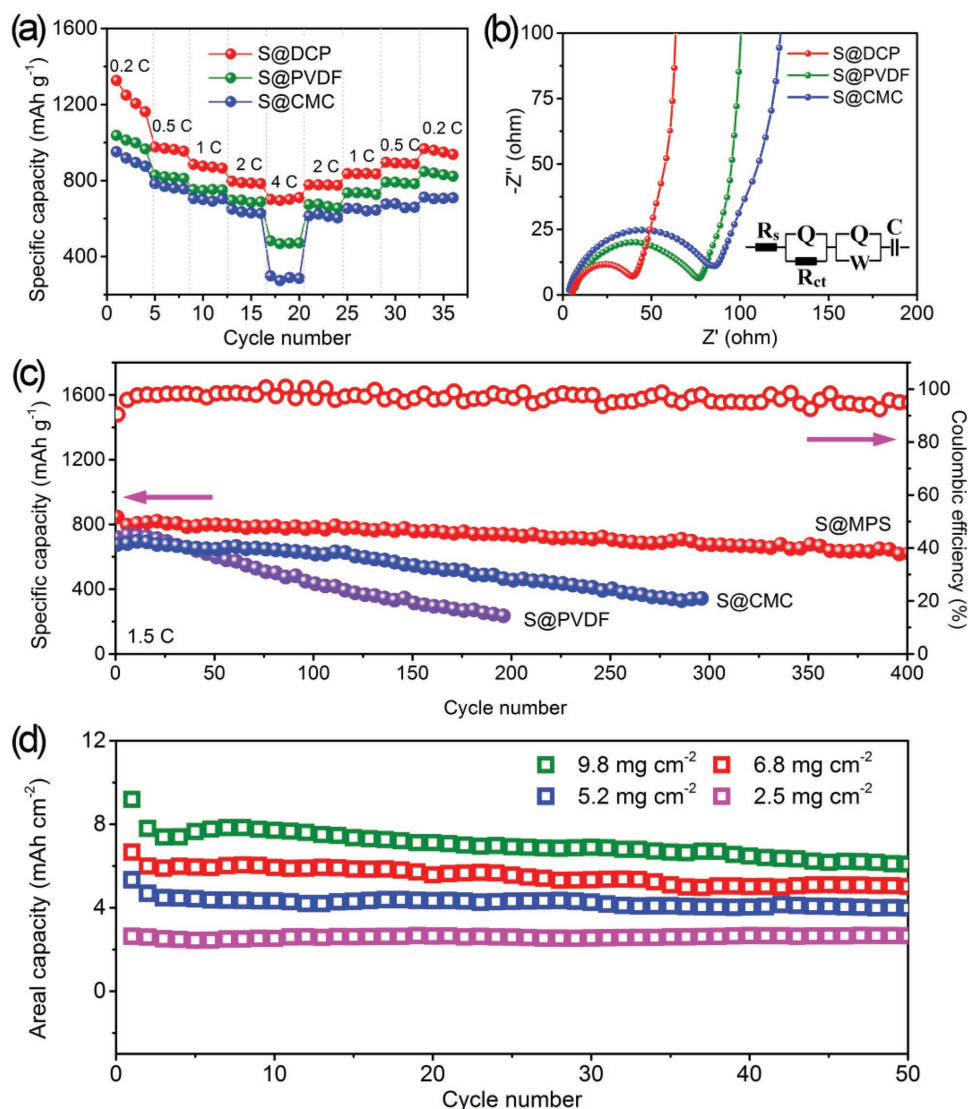


**Figure 3.** a) Rate capability of the cells assembled with DCP, CMC, and PVDF binder at various current densities from 0.2 to 4 C. b) Electrochemical impedance spectra of the cells assembled with DCP, CMC, and PVDF binder (Inset is the equivalent circuits). c) The cycling performance of the sulfur electrodes based on DCP, CMC, and PVDF binder. d) The cycling stability of S@DCP cathodes with sulfur loadings of 2.5, 5.2, 6.8, and 9.8 mg cm<sup>-2</sup> at 0.5 mA cm<sup>-2</sup>.

order to further demonstrate the prominent electrochemical properties, electrochemical impedance spectroscopy measurements of S@DCP, S@PVDF, and S@CMC were carried out in Figure 3b. The Nyquist plots of these cathodes are composed of one depressed semicircle in the high-frequency region and an inclined line at low-frequency region, which is due to the charge transfer resistance ( $R_{ct}$ ) and a mass transfer process.<sup>[17]</sup> The high-frequency intercept on the real axis represents the ohmic resistance ( $R_s$ ) of the cell. The fitted  $R_s$  and  $R_{ct}$  values are shown in Table S1 (Supporting Information). It can be found that the value of  $R_{ct}$  for S@DCP (33.73  $\Omega$ ) is much lower than those of S@PVDF (66.51  $\Omega$ ) and S@CMC (76.46  $\Omega$ ), which means that the S@DCP cathode exhibits faster charge transfer compared to that of the other electrodes. Besides, the evolution of different cathode impedance has been measured after 1 and 10 cycles. As shown in Figure S6 (Supporting Information),

the S@DCP exhibits more stable and much lower resistance, demonstrating stable composite structure and fast electrode kinetics.<sup>[18]</sup> However, the resistance values of S@CMC and S@PVDF rise clearly after 10 cycles compared with that at the first cycle, indicating the serious depositing and aggregating process on the surface of electrode.<sup>[19]</sup> Galvanostatic cycling was further carried out to investigate the benefits of DCP binder on Li-S batteries. Figure 3c shows the long-term cycling stability of the S@DCP cathode tested at a current density of 1.5 C. The cell delivers an initial capacity of 845.2 mAh g<sup>-1</sup>. After 400 cycles, the capacity stabilizes at 649.2 mAh g<sup>-1</sup> with a low capacity fade rate of 0.058% per cycle. Postmortem scanning electron microscopy (SEM) was conducted to distinguish the difference in the morphology of S@DCP, S@PVDF, and S@CMC cathodes before and after cycling (Figure S7, Supporting Information). Before cycling, all of the S@DCP,

S@PVDF, and S@CMC cathodes exhibit typical porous surface containing well-distributed sulfur particles. However, after 100 cycles, the surfaces of S@PVDF and S@CMC are covered with solid films, which is due to the irregular precipitations of sulfur species in pores of the particles and between the particles. In contrast, the S@DCP cathode could still maintain similar porous structure after cycling.

Generally, it is critical to construct high sulfur loading electrodes for the purpose of building high-energy-density Li-S batteries. Therefore, electrodes with varied sulfur loadings (2.5–9.8 mg cm<sup>-2</sup>) were prepared to investigate the advantage of DCP binder in the construction of high sulfur mass loading. Moreover, although high electrolyte/sulfur ratio is necessary to fully wet the high reaction surface areas, it comes at the sacrifice of the practical electrochemical performances and energy density of the batteries.<sup>[20]</sup> Thus a low electrolyte/sulfur ratio (5:1, μL: mg) was used to maximize the overall energy density. Figure S8 (Supporting Information) shows the voltage profiles of the electrodes at a current density of 0.5 mA cm<sup>-2</sup>. All the high-loading sulfur electrodes show the typical curves of conventional Li-S batteries. Specific capacities of 1040.1, 1019.2, 970.6, and 938.8 mAh g<sup>-1</sup> were achieved for the thick electrodes

with high loadings of 2.5, 5.2, 6.8, and 9.8 mg cm<sup>-2</sup>, corresponding to areal capacities of 2.6, 5.3, 6.6, and 9.2 mAh cm<sup>-2</sup> (Figure 3d; Figure S9, Supporting Information). Long-term cycling stability was further conducted at a slow cycling rate of 0.3 C in Figure S10 (Supporting Information), exhibiting excellent capacity retention of 90.5% after 200 cycles. These results indicate that DCP binder not only endows the entire sulfur-based cathode with enhanced conductivity but also effectively confines the soluble polysulfide within the electrode.

To further understand electrochemical properties of S@DCP cathode, in situ X-ray diffraction (XRD) was conducted. Special design of Li-S batteries enables us to realize the real-time monitoring of the local structural and chemical evolution of S@DCP cathode during the charge–discharge process (Figure 4a). As shown in Figure 4b,c, the main peaks in the range of 20°–24° are derived from the decomposition of electrolyte (Li<sub>2</sub>CO<sub>3</sub> and Li<sub>2</sub>SO<sub>x</sub>),<sup>[21]</sup> which remained almost unchanged during the whole charge–discharge process. The peaks associated with (2 2 2), (3 1 1), (0 4 0), and (3 1 3) reveal the different crystalline planes of S<sub>8</sub>, which decrease during the discharge process, indicating the sufficient reaction between S<sub>8</sub> and lithium ions.<sup>[22]</sup> This can be further demonstrated by the color change presented in the

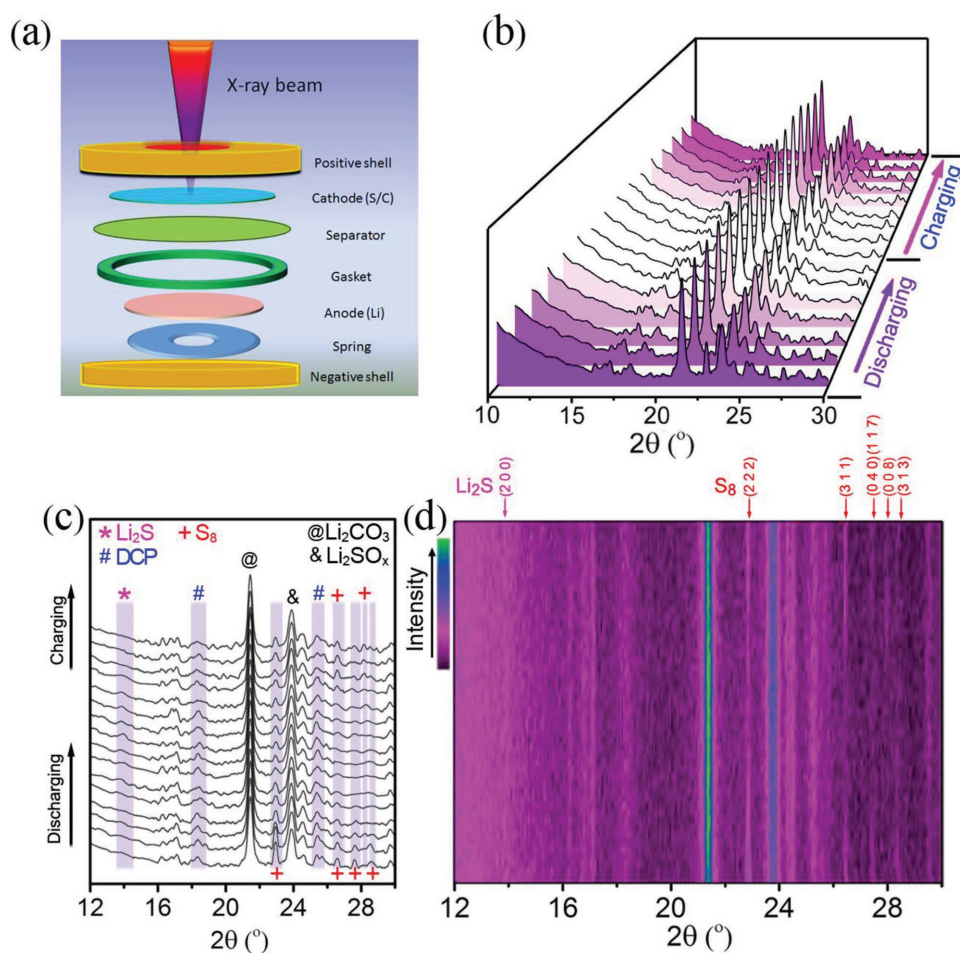


**Figure 4.** a) Schematic illustration of the cell component for in situ XRD measurement. b) In situ XRD patterns evolution during initial cycle at a current rate of 0.1 C. c) In situ XRD patterns extracted from Figure 3b, showing the structural and chemical evolution of S@DCP cathode. d) The contour plot of in situ XRD patterns collected during the initial cycle.

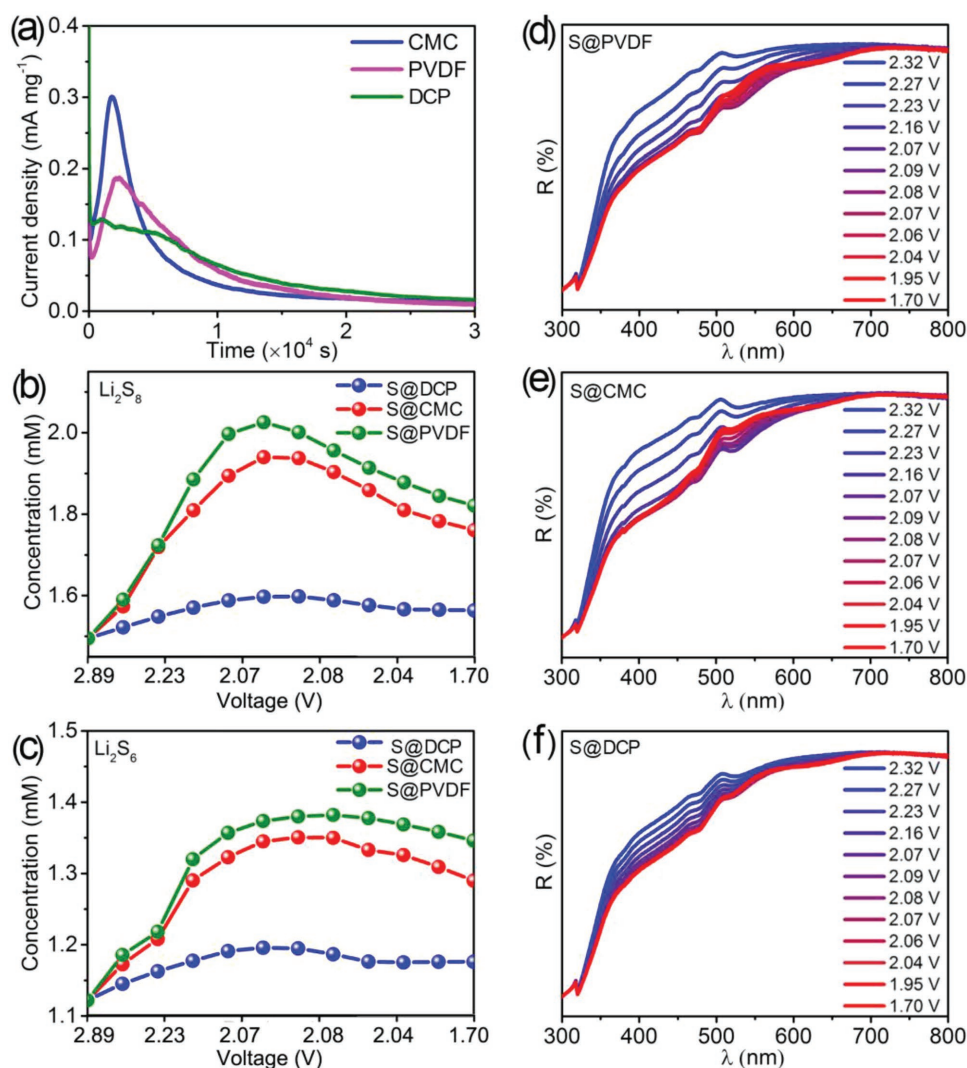


**Figure 5.** a) Potentiostatic discharge curves of  $\text{Li}_2\text{S}_8$ /DOL/DME solution at 2.1 V with various binders, including CMC, PVDF, and DCP. Quantitative evaluation of the concentration evolution of b)  $\text{Li}_2\text{S}_8$  and c)  $\text{Li}_2\text{S}_6$  at different discharge potentials. All the concentration values are calculated based on UV-vis spectra of the batteries assembled with d) S@PVDF cathode, e) S@CMC cathode, and f) S@DCP cathode between  $\lambda = 300\text{--}800 \text{ nm}$ .

contour plot of in situ XRD patterns (Figure 4d). During the discharge process, the XRD peaks of  $\text{S}_8$  (marked by red arrow) are gradually weakened, while the peak associated with  $\text{Li}_2\text{S}$  (marked by pink arrow) increases. Upon the following charge process, the intensity of  $\text{Li}_2\text{S}$  peak decreases progressively and the reappearance of  $\text{S}$  peaks toward the end of the cycle can be observed in the XRD patterns and the corresponding contour plot. However, for S@PVDF and S@CMC, the intensity of the  $\text{S}_8$  peaks decreases and finally vanishes during the discharge process, indicating the sufficient reaction between  $\text{S}_8$  and lithium ions. When the charge proceeds, the intensities of  $\text{S}_8$  remained weak, which are related to the formation of soluble sulfur species that does not recrystallize on the electrode. In addition, the structural stability of DCP binder during the whole charge-discharge process is also demonstrated. As shown in Figure 4c, the signals of DCP binder appear at the beginning of discharge process and the intensities of these peaks remain unchanged. This demonstrates that the DCP binder can retain

the crystalline structure, which is beneficial to the conductivity of S@DCP cathode.

The interaction between binders and soluble polysulfide impacts greatly on the interfacial polysulfide redox and  $\text{Li}_2\text{S}$  deposition. Accordingly, we study the kinetics of  $\text{Li}_2\text{S}$  nucleation by potentiostatically discharging  $\text{Li}_2\text{S}_8$ /1,3-dioxolane/1,2-dimethoxyethane catholyte at 2.1 V on various binders, including CMC, PVDF, and DCP, respectively. It is known that  $\text{Li}_2\text{S}$  was electrodeposited onto cathodes below the equilibrium potential. Thus it is reasonable to monitor the deposition of polysulfide by current flow.<sup>[23]</sup> As shown in Figure 5a, the potentiostatic currents for all three binders reached the maximum value at  $\approx 1500 \text{ s}$ . However, in stark contrast to the clear and strong current peaks for CMC and PVDF, DCP exhibits no such great peak intensity, indicating the effective prevention of the early precipitation of  $\text{Li}_2\text{S}$ .

As an effective tool to monitor the evolution of polysulfide intermediates during battery cycling,<sup>[24]</sup> in situ UV-Vis

spectroscopy was conducted to quantitatively analyze the effect of different binders (DCP, CMC, and PVDF) on electrochemical performance. The characteristic wavelengths of different polysulfide species have been determined in our previous report.<sup>[25]</sup> It is found that the derivatives at  $\lambda = 570$  and  $530$  nm correspond to the long-chain polysulfide of  $\text{Li}_2\text{S}_8$  and  $\text{Li}_2\text{S}_6$ , respectively. The derivative located at  $510$  nm is attributed to the mid-chain polysulfide of  $\text{Li}_2\text{S}_4$ . The derivative peak of short-chain polysulfide is found at  $450$  nm. Correlations between concentrations and normalized reflectance of polysulfide ( $\text{Li}_2\text{S}_x$ ,  $2 \leq x \leq 8$ ) were systematically studied as follows: 1) from the measured spectra, the intensities of the reflection for polysulfide ( $\text{Li}_2\text{S}_x$ ,  $2 \leq x \leq 8$ ) at preselected wavelengths are collected. 2) The intensity of the first spectrum is normalized to 1, and subsequently collected intensities at preselected wavelengths are normalized based on the first spectrum. 3) Then normalized intensities of shorter wavelengths are subtracted by the values of longer wavelengths. The evolution of concentrations of different types of polysulfide can be calculated according to the linear fits of the normalized intensities measured with different concentrations of the polysulfides, as determined in our previous report. Figure 5b,c shows the comparison results of the concentration changes of the lithium polysulfide in the electrolyte, which are calculated based on UV-vis spectra of the batteries assembled with S@PVDF, S@CMC, and S@DCP cathode (Figure 5d-f). It is obvious that the concentrations of polysulfide for all the cathodes (S@PVDF, S@CMC, and S@DCP) are at the same level in the beginning but soon show the obvious difference. Significant increases in the polysulfide concentrations can be observed for S@PVDF and S@CMC. In contrast, there is little change in the polysulfide concentration, which keeps a small value throughout the discharge process in S@DCP-based cell. Further experiments to confirm that DCP restricts the migration of negatively charged polysulfides are shown in Figures S12 and S13 (Supporting Information). It can be clearly seen in Figure S12 (Supporting Information) that the separators from S@CMC- and S@PVDF-based cell show conspicuous yellow color in a large area, implying that a large amount of polysulfides were diffused from the cathode. For comparison, the trace of the dissolved polysulfides on the separator from S@DCP-based cells at the discharge states of  $2.27$  and  $2.09$  V show light yellow color, illustrating the effective trapping of polysulfide in the S@DCP cathodes during discharge process. In situ visual-electrochemical study was also examined to illustrate polymer-polysulfide interactions. As shown in Figure S13 (Supporting Information), due to the released polysulfides, the increasingly changed color of electrolyte from colorless to green-yellow is observed for the S@PVDF and S@CMC cathodes, contrary to the constantly colorless electrolytes for the S@DCP cathode.

In conclusion, we have developed a novel binder by entangling conductive Sul-PPy chains onto the adhesive CMC matrix. The DCP binder is shown to assist the interparticle physical connection as well as improved  $\text{Li}^+/\text{e}^-$  transportation, leading to high sulfur loading, superior rate performance, and excellent cycling stability. Particularly, the thick electrode with up to  $9.8 \text{ mg cm}^{-2}$  sulfur loading delivers a high area capacity of  $9.2 \text{ mAh cm}^{-2}$  at a low electrolyte/sulfur ratio ( $5:1$ ,  $\mu\text{L mg}^{-1}$ ). The sulfur reduction/recrystallization occurred during the

cycling can be confirmed by in situ XRD analysis, accompanied with the structural stability of DCP binder. Additionally, the dissolved polysulfide intermediates can be effectively confined in the cathode, which is due to the repulsive effect of sulfonate anion groups bound on the polymer backbone and can be further proven by in situ UV-vis measurements. This achievement might open a new area for the design of multifunctional binders for high sulfur loading Li-S batteries.

## Supporting Information

Supporting Information is available from the Wiley Online Library or directly from the author.

## Acknowledgements

This work was financially supported by the National Natural Science Foundation of China (No. 21703149 and No. 51622208).

## Conflict of Interest

The authors declare no conflict of interest.

## Keywords

double-chain polymer network, high sulfur loading, in situ measurements, low electrolyte/sulfur ratio

Received: April 23, 2018

Revised: June 18, 2018

Published online: July 20, 2018

- [1] a) S. Urbonaite, T. Poux, P. Novák, *Adv. Energy Mater.* **2015**, *5*, 1500118; b) F. Zhou, Z. Li, X. Luo, T. Wu, B. Jiang, L. L. Lu, H. B. Yao, M. Antonietti, S. H. Yu, *Nano Lett.* **2018**, *18*, 1035; c) R. P. Fang, S. Y. Zhao, Z. H. Sun, D. W. Wang, H. M. Cheng, F. Li, *Adv. Mater.* **2017**, *29*, 1606823; d) L. Li, L. Chen, S. Mukherjee, J. Gao, H. Sun, Z. B. Liu, X. L. Ma, T. Gupta, C. V. Singh, W. C. Ren, H. M. Cheng, N. Koratkar, *Adv. Mater.* **2017**, *29*, 1602734; e) F. X. Wu, S. Q. Chen, V. Srot, Y. Y. Huang, S. K. Sinha, P. A. van Aken, J. Maier, Y. Yu, *Adv. Mater.* **2018**, *30*, 1706643.
- [2] a) Z. W. Seh, Y. M. Sun, Q. Zhang, Y. Cui, *Chem. Soc. Rev.* **2016**, *45*, 5605; b) Y. Yang, G. Y. Zheng, Y. Cui, *Chem. Soc. Rev.* **2013**, *42*, 3018; c) J. Liu, M. H. Sun, Q. Zhang, F. F. Dong, P. Kaghazchi, Y. X. Fang, S. Q. Zhang, Z. Lin, *J. Mater. Chem. A* **2018**, *6*, 7382; d) Y. C. Jeong, J. H. Kim, S. Nam, C. R. Park, S. J. Yang, *Adv. Funct. Mater.* **2018**, *28*, 1707411.
- [3] a) S. H. Chung, C. H. Chang, A. Manthiram, *Energy Environ. Sci.* **2016**, *9*, 3188; b) J. X. Song, T. Xu, M. L. Gordin, P. Y. Zhu, D. P. Lv, Y. B. Jiang, Y. S. Chen, Y. H. Duan, D. H. Wang, *Adv. Funct. Mater.* **2014**, *24*, 1243; c) L. X. Miao, W. K. Wang, K. G. Yuan, Y. S. Yang, A. B. Wang, *Chem. Commun.* **2014**, *50*, 13231.
- [4] a) J. Liu, D. G. D. Galpaya, L. J. Yan, M. H. Sun, Z. Lin, C. Yan, C. D. Liang, S. Q. Zhang, *Energy Environ. Sci.* **2017**, *10*, 750; b) X. F. Yang, Y. Q. Chen, M. R. Wang, H. Z. Zhang, X. F. Li, H. M. Zhang, *Adv. Funct. Mater.* **2016**, *26*, 8427.
- [5] Q. Pang, X. Liang, C. Y. Kwok, J. Kulisch, L. F. Nazar, *Adv. Energy Mater.* **2017**, *7*, 1601630.

- [6] a) H. Q. Wang, V. Sencadas, G. P. Gao, H. Gao, A. J. Du, H. K. Liu, Z. P. Guo, *Nano Energy* **2016**, *26*, 722; b) W. Chen, T. Qian, J. Xiong, N. Xu, X. J. Liu, J. Liu, J. Q. Zhou, X. W. Shen, T. Z. Yang, Y. Chen, C. L. Yan, *Adv. Mater* **2017**, *29*, 1605160.
- [7] G. R. Li, M. Ling, Y. F. Ye, Z. P. Li, J. h. Guo, Y. F. Yao, J. F. Zhu, Z. Lin, S. Q. Zhang, *Adv. Energy Mater.* **2015**, *5*, 1500878.
- [8] J. L. Wang, Z. D. Yao, C. W. Monroe, J. Yang, Y. Nuli, *Adv. Funct. Mater.* **2013**, *23*, 1194.
- [9] M. J. Lacey, F. Jeschull, K. Edström, D. Brandell, *J. Power Sources* **2014**, *264*, 8.
- [10] Q. Q. Wang, W. K. Wang, Y. Q. Huang, F. Wang, H. Zhang, Z. B. Yu, A. B. Wang, K. G. Yuan, *J. Electrochem. Soc.* **2011**, *158*, A775.
- [11] a) G. M. Zhou, K. Liu, Y. C. Fan, M. Q. Yuan, B. F. Liu, W. Liu, F. F. Shi, Y. Y. Liu, W. Chen, J. Lopez, D. Zhuo, J. Zhao, Y. Tsao, X. Y. Huang, Q. F. Zhang, Y. Cui, *ACS Cent. Sci.* **2018**, *4*, 260; b) W. W. Zeng, L. Wang, X. Peng, T. F. Liu, Y. Y. Jiang, F. Qin, L. Hu, P. K. Chu, K. F. Huo, Y. H. Zhou, *Adv. Energy Mater.* **2018**, *8*, 1702314.
- [12] a) R. J. Lin, A. Li, L. B. Lu, Y. Cao, *Carbohydr. Polym.* **2015**, *118*, 126; b) D. R. Biswal, R. P. Singh, *Carbohydr. Polym.* **2004**, *57*, 379.
- [13] Y. Z. Fu, A. Manthiram, *Chem. Mater.* **2012**, *24*, 3081.
- [14] H. J. Lee, Y. R. Jo, H. J. Li, Z. B. Zhao, H. Bin Wu, C. Hao, S. H. Liu, B. J. Kim, J.-S. Lee, *Nat. Commun.* **2016**, *7*, 12803.
- [15] a) T. Yim, S. J. Choi, Y. N. Jo, T.-H. Kim, K. J. Kim, G. Jeong, Y.-J. Kim, *Electrochim. Acta* **2014**, *136*, 112; b) Z. A. Zhang, T. Zeng, Y. Q. Lai, M. Jia, J. Li, *J. Power Sources* **2014**, *247*, 1.
- [16] a) H. Hu, H. Y. Cheng, Z. F. Liu, G. J. Li, Q. C. Zhu, Y. Yu, *Nano Lett.* **2015**, *15*, 5116; b) Y. G. Zhang, Y. Zhao, A. Yermukhambetova, Z. Bakenov, P. Chen, *J. Mater. Chem. A* **2013**, *1*, 295.
- [17] G. M. Zhou, S. F. Pei, L. Li, D.-W. Wang, S. G. Wang, K. Huang, L.-C. Yin, F. Li, H.-M. Cheng, *Adv. Mater* **2014**, *26*, 625.
- [18] X. L. Wang, G. Li, J. D. Li, Y. N. Zhang, A. Wook, A. P. Yu, Z. W. Chen, *Energy Environ. Sci.* **2016**, *9*, 2533.
- [19] G. Q. Ma, Z. Y. Wen, J. Jin, Y. Lu, K. Rui, X. W. Wu, M. F. Wu, J. C. Zhang, *J. Power Sources* **2014**, *254*, 353.
- [20] a) S.-H. Chung, A. Manthiram, *Adv. Mater* **2018**, *30*, 1705951; b) J. M. Zheng, D. P. Lv, M. Gu, C. M. Wang, J. G. Zhang, J. Liu, J. Xiao, *J. Electrochem. Soc.* **2013**, *160*, A2288.
- [21] J. Liu, T. Qian, M. F. Wang, J. Q. Zhou, N. Xu, C. L. Yan, *Nano Lett.* **2018**, *18*, 4598.
- [22] N. A. Cañas, S. Wolf, N. Wagner, K. A. Friedrich, *J. Power Sources* **2013**, *226*, 313.
- [23] a) D. Moy, A. Manivannan, S. R. Narayanan, *J. Electrochem. Soc.* **2015**, *162*, A1; b) C. Y. Chen, H. J. Peng, T. Z. Hou, P. Y. Zhai, B. Q. Li, C. Tang, W. C. Zhu, J. Q. Huang, Q. Zhang, *Adv. Mater* **2017**, *29*, 1606802.
- [24] a) M. U. M. Patel, R. Demir-Cakan, M. Morcrette, J. M. Tarascon, M. Gaberscek, R. Dominko, *ChemSusChem* **2013**, *6*, 1177; b) M. U. M. Patel, R. Dominko, *ChemSusChem* **2014**, *7*, 2167.
- [25] a) N. Xu, T. Qian, X. J. Liu, J. Liu, Y. Chen, C. L. Yan, *Nano Lett.* **2017**, *17*, 538; b) J. Liu, T. Qian, M. F. Wang, X. J. Liu, N. Xu, Y. Z. You, C. L. Yan, *Nano Lett.* **2017**, *17*, 5064.